

Photonic sensing of arterial distension

DOMINIC RUH,^{1,*} SIVARAMAN SUBRAMANIAN,¹ STANISLAV SHERMAN,¹ JOHANNES RUHHAMMER,¹ MICHAEL THEODOR,¹ DIRK LEBRECHT,² KATHARINA FOERSTER,³ CLAUDIA HEILMANN,³ FRIEDHELM BEYERSDORF,³ HANS ZAPPE,¹ AND ANDREAS SEIFERT^{1,4}

¹*Department of Microsystems Engineering – IMTEK, University of Freiburg, Germany*

²*Department of Rheumatology and Clinical Immunology, University Medical Center Freiburg, Germany*

³*Department of Cardiovascular Surgery, Heart Center, University of Freiburg, Germany*

⁴*CIC nanoGUNE, San Sebastián, Spain*

*dominic.ruh@imtek.uni-freiburg.de

Abstract: Most cardiovascular diseases, such as arteriosclerosis and hypertension, are directly linked to pathological changes in hemodynamics, i.e. the complex coupling of blood pressure, blood flow and arterial distension. To improve the current understanding of cardiovascular diseases and pave the way for novel cardiovascular diagnostics, innovative tools are required that measure pressure, flow, and distension waveforms with yet unattained spatiotemporal resolution. In this context, miniaturized implantable solutions for continuously measuring these parameters over the long-term are of particular interest. We present here an implantable photonic sensor system capable of sensing arterial wall movements of a few hundred microns *in vivo* with sub-micron resolution, a precision in the micrometer range and a temporal resolution of 10 kHz. The photonic measurement principle is based on transmission photoplethysmography with stretchable optoelectronic sensors applied directly to large systemic arteries. The presented photonic sensor system expands the toolbox of cardiovascular measurement techniques and makes these key vital parameters continuously accessible over the long-term. In the near term, this new approach offers a tool for clinical research, and as a perspective, a continuous long-term monitoring system that enables novel diagnostic methods in arteriosclerosis and hypertension research that follow the trend in quantifying cardiovascular diseases by measuring arterial stiffness and more generally analyzing pulse contours.

© 2016 Optical Society of America

OCIS codes: (170.4580) Optical diagnostics for medicine, (170.0170) Medical optics and biotechnology, (170.3660) Light propagation in tissues, (170.4580) Optical diagnostics for medicine, (230.3990) Micro-optical devices. (230.4685) Optical microelectromechanical devices. (280.4788) Optical sensing and sensors.

References and links

1. J. A. Rogers, T. Someya, Y. Huang, "Materials and mechanics for stretchable electronics," *Science* **327**, 1603–1607 (2010).
2. D. Ruh, P. Reith, S. Sherman, M. Theodor, J. Ruhhammer, A. Seifert, H. Zappe, "Stretchable optoelectronic circuits embedded in a polymer network," *Adv. Mater.* **26**, 1706–1710 (2014).
3. D.-H. Kim, R. Ghaffari, N. Lu, S. Wang, S.P. Lee, H. Keume, R. D'Angelo, L. Klinker, Y. Su, C. Lu, Y.-S. Kim, A. Ameen, Y. Li, Y. Zhang, B. de Graff, Y.-Y. Hsu, Z. Liu, J. Ruskin, L. Xu, C. Lu, F.G. Omenetto, Y. Huang, M. Mansour, M.J. Slepian and J.A. Rogers, "Electronic Sensor and Actuator Webs for Large-Area Complex Geometry Cardiac Mapping and Therapy," *Proceedings of the National Academy of Sciences USA* **109** 19910–19915 (2012).
4. S.R. Gutbrod, M.S. Sulkin, J.A. Rogers and I.R. Efimov, "Patient-Specific Flexible and Stretchable Devices for Cardiac Diagnostics and Therapy," *Progress in Biophysics and Molecular Biology* **115**, 244–251 (2014).
5. M. Theodor, D. Ruh, J. Fiala, K. Förster, C. Heilmann, Y. Manoli, F. Beyersdorf, H. Zappe, A. Seifert, "Subcutaneous blood pressure monitoring with an implantable optical sensor," *Biomed. Microdevices* **15**, 811–820 (2013).
6. J. Fiala, P. Bingger, D. Ruh, K. Förster, C. Heilmann, F. Beyersdorf, H. Zappe, A. Seifert, "An implantable optical blood pressure sensor based on pulse transit time," *Biomed. Microdevices* **15**, 73–81 (2013).
7. J. A. Potkay, "Long term, implantable blood pressure monitoring systems," *Biomed. Microdevices* **10**, 379–392 (2008).
8. E. O. Ofili, A. J. Labovitz, M. J. Kern, "Coronary flow velocity dynamics in normal and diseased arteries," *Am. J. Cardiol.* **71**, 3D–9D (1993).

9. F. A. Lupotti, F. Mastik, S. G. Carlier, E. I. Cespedes, A. F. W. van der Steen, "Quantitative IVUS blood flow using an array catheter," *Computers in Cardiology* 2001, 5–8 (2001).
10. A. Lotfi, A. Jeremias, W. F. Fearon, M. D. Feldman, R. Mehran, J. C. Messenger, C. L. Grines, L. S. Dean, M. J. Kern, L. W. Klein, "Expert consensus statement on the use of fractional flow reserve, intravascular ultrasound, and optical coherence tomography," *Catheter Cardiovasc. Interv.* **83**, 509–518 (2014).
11. W. W. Nichols, M. F. O'Rourke, C. Vlachopoulos, *McDonald's Blood Flow in Arteries: Theoretical, Experimental and Clinical Principles* (Hodder Arnold, 2011).
12. R. L. Armentano, J. G. Barra, J. Levenson, A. Simon, R. H. Pichel, "Arterial wall mechanics in conscious dogs: Assessment of viscous, inertial, and elastic moduli to characterize aortic wall behavior," *Circ. Res.* **76**, 468–478 (1995).
13. P. Kruizinga, F. Mastik, S. C. H. van den Oord, A. F. L. Schinkel, J. G. Bosch, N. de Jong, G. van Soest, A. F. W. van der Steen, "High-definition imaging of carotid artery wall dynamics," *Ultrasound Med. Biol.* **40**, 2392–2403 (2014).
14. W. Kong, D. Rollins, R. Ideker, W. Smith, "Design and initial evaluation of an implantable sonomicrometer and cw doppler flowmeter for simultaneous recordings with a multichannel telemetry system," *IEEE Trans. Biomed. Eng.* **52**, 1365–1367 (2005).
15. D. H. Kim, N. Lu, R. Ghaffari, Y.-S. Kim, S. P. Lee, L. Xu, J. Wu, R.-H. Kim, J. Song, Z. Liu, and others, "Materials for multifunctional balloon catheters with capabilities in cardiac electrophysiological mapping and ablation therapy," *Nat. Mater.* **10**, 316–323 (2011).
16. S. Laurent, J. Cockcroft, L. Van Bortel, P. Boutouyrie, C. Giannattasio, D. Hayoz, B. Pannier, C. Vlachopoulos, I. Wilkinson, H. Struijker-Boudier, "Expert consensus document on arterial stiffness: methodological issues and clinical applications," *Eur. Heart. J.* **27**, 2588–2605 (2006).
17. D. Ruh, S. Subramanian, M. Theodor, H. Zappe, A. Seifert, "Radiative transport in large arteries," *Biomed. Opt. Express* **5**, 54–68 (2014).
18. M. Couade, M. Pernot, C. Prada, E. Messas, J. Emmerich, P. Bruneval, A. Criton, M. Fink, M. Tanter, "Quantitative assessment of arterial wall biomechanical properties using shear wave imaging," *Ultrasound Med. Biol.* **36**, 1662–1676 (2010).
19. P. Tortoli, T. Morganti, G. Bambi, C. Palombo, K. V. Ramnarine, "Noninvasive simultaneous assessment of wall shear rate and wall distension in carotid arteries," *Ultrasound Med. Biol.* **32**, 1661–1670 (2006).
20. B. Rubehn, C. Bosman, R. Oostenveld, P. Fries, T. Stieglitz, "A MEMS-based flexible multichannel ECoG-electrode array," *J. Neural. Eng.* **6**, 036003 (2009).
21. J. Ruhlhammer, D. Ruh, K. Förster, C. Heilmann, F. Beyersdorf, A. Barker, B. Jung, A. Seifert, F. Goldschmidtboeing, P. Woias, "Arterial strain measurement by implantable capacitive sensor without vessel constriction," In *Proceedings of IEEE Conference on Engineering in Medicine and Biology Society (EMBC)*, 535–538 (2012).
22. L. H. Peterson, R. E. Jensen, J. Parnell, "Mechanical properties of arteries in vivo," *Circ. Res.* **8**, 622–639 (1960).
23. L. Wolff, P. Fernandez, K. Kroy, "Resolving the Stiffening-Softening Paradox in Cell Mechanics," *PLOS one* **7**, e40063 (2012).
24. R. H. Cox, "Wave propagation through a Newtonian fluid contained within a thick-walled, viscoelastic tube," *Biophys. J.* **8**, 691 (1968).
25. D. J. Korteweg, "Ueber die Fortpflanzungsgeschwindigkeit des Schalles in elastischen Röhren," *Annalen der Physik* **241**, 525–542 (1878).
26. M. Theodor, J. Fiala, D. Ruh, K. Förster, C. Heilmann, F. Beyersdorf, Y. Manoli, H. Zappe, and A. Seifert, "Implantable Accelerometer System for the Determination of Blood Pressure Using Reflected Wave Transit Time," *Sensors and Actuators A: Physical* **206**, 151–158 (2014).
27. M. Meinke, G. Müller, J. Helfmann, M. Friebe, "Empirical model functions to calculate hematocrit-dependent optical properties of human blood," *Appl. Opt.* **46**, 1742–1753 (2007).
28. M. Keijzer, S. L. Jacques, S. A. Prahl, A. J. Welch, "Light distributions in artery tissue: Monte Carlo simulations for finite-diameter laser beams," *Lasers Surg. Med.* **9**, 148–154 (1989).

1. Introduction

The development of flexible and stretchable sensor systems that comply with the soft mechanical properties of tissue opens new ways in biomedical engineering [1, 2]. Especially implantable devices that act on or sense the cardiovascular system are challenging in that regard, since they have to conform to the pulsatile nature of the cardiovascular system [3, 4]. Implantable sensor systems for measuring pulse waveforms have been demonstrated [5, 6], however, in contrast to the numerous sensors to access pressure [7] and flow [8–10], implantable systems measuring arterial distension are still in an early stage. The reason behind is simple: while arteries distend only by a few percent of their diameter, pressure and flow vary by 50 to 100 % over a cardiac cycle [11]. Hence, sensing and accurately resolving the microscopic arterial distensions of about 250 μm is much more challenging than sensing pressure and flow.

There exists only one implantable solution, known as sonomicrometry capable of measuring arterial distension *in vivo* [11]. Sonomicrometry estimates arterial distension from the transit time of an ultrasonic pulse traveling between two piezo-crystals that are diametrically placed at the arterial wall using surgical sutures [12]. The resolution of these commercially available systems (e.g. Sonometrics Corporation, Ontario, Canada) is determined by the frequency of the ultrasound pulse and is intrinsically limited to 12 – 24 microns, which is insufficient to record the smallest features of the arterial wall waveform of sub-micrometer dimensions [13]. Furthermore, high energy consumption [14] and damage to the arterial wall due to surgical sutures make sonomicrometry impractical for continuous long-term monitoring.

In this paper, we present a novel implantable photonic measurement system capable of sensing arterial distension *in vivo* with sub-micron resolution, a precision in the single-digit micron range, and a temporal resolution of 10 kHz. The photonic measurement principle of the presented sensor system is based on transmission photoplethysmography (PPG). However, in contrast to standard clinical practice, the measurement site of the PPG is moved from the fingertip or earlobe directly to large arteries. It is realized by the fabrication of a miniaturized, stretchable photoplethysmograph that is inspired by recent advancements in the field of stretchable electronics [2, 15]. The capability of this sensor system in measuring arterial distension is presented by *in vitro* and *in vivo* experiments. The results show that the developed implantable photonic sensor can measure arterial distension even under extreme vital conditions. Furthermore, the distension data gives new insight into the biomechanics of the arterial wall and hence provides an implantable solution to quantify the key risk factor for cardiovascular events, arterial stiffness [16].

2. Simulations on photoplethysmography at large arteries

Photoplethysmography at large arteries is performed by detecting a change in amount of photons transmitted across a distending artery over a cardiac cycle. A theoretical study on light propagation in large blood-filled arteries that solves stochastically the radiative transfer equation on layered cylindrical geometries by means of Monte-Carlo simulations was previously published by the same authors [17] and forms the basis for all simulation data presented throughout this paper. Further details on the simulation are given in Section 1 of the appendix.

Figure 1(a) shows the three-dimensional steady-state simulation scheme including the decay of radiant flux inside the model artery as well as the positions of light source and photodetector. PPGs were computed by distending the model artery in discrete steps of 0.5 % corresponding to different strain states, and extracting the amount of photons from a Lambertian emitter reaching the photodetector. Three different model arteries with diameters of 2.4, 3.3 and 4.8 mm were considered to investigate most common systemic arteries such as carotid, femoral and brachial. To assure that a significant number of photons reach the photodetector, the wavelengths chosen for which blood shows low absorbance are 660 nm (red) and 880 nm (infrared). With these parameters, the following paragraphs show the characteristics of the measurement principle in terms of linearity, sensitivity and signal-to-noise ratio.

Linearity. The graphs in Fig. 1 (b) show the correlation between the normalized optical flux Φ_{norm} reaching the photodetector and the arterial diameter z for three different rest diameters at two wavelengths. The linear relationship between Φ_{norm} and z is quantified by the coefficient of determination, $R^2 \geq 0.9958$ for the red wavelength and $R^2 \geq 0.9924$ for the infrared wavelength.

This linearity can be explained analytically by assuming the radiant flux decay to be linear in the range of the small arterial distensions. The first order approximation of the Taylor series expansion of the normalized radiant flux decay around the rest diameter of the artery reads,

$$\Phi_{norm}(z) = \frac{\Phi(z)}{\Phi(z_0)} = 1 + \frac{1}{\Phi(z_0)} \left. \frac{\delta\Phi(z)}{\delta z} \right|_{z=z_0} (z - z_0) + R(z), \quad (1)$$

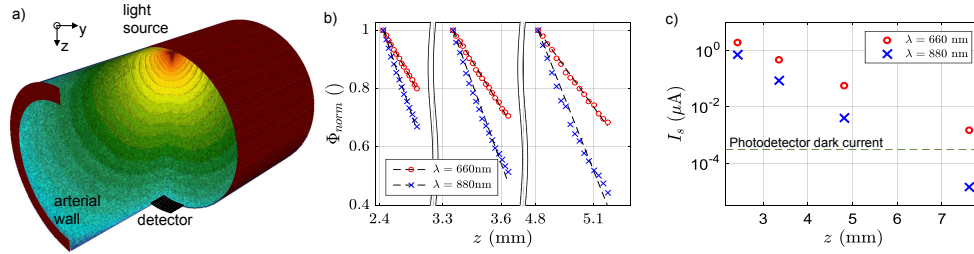


Fig. 1. Simulated light propagation in an artery. **a)** 3-dimensional radiant flux distribution in an arterial segment. The contours depict the decay of the radiant flux from maximum (red) at the point of input to the least (blue) at the far end of the segment. The reddish pattern depicts the arterial wall. **b)** Calculated optical output normalized with respect to the output at zero distension as a function of arterial distension for three different initial arterial diameters of 2.4, 3.3, and 4.8 mm; red circles at a wavelength of 660 nm and blue crosses at 880 nm; lines show the linear fits to the underlying data. **c)** Simulated photocurrent for the photodetector with a responsivity of 0.5 A/W from a 5 mW light source for different arterial diameters. The green dashed line shows the photodetector dark current of a standard photodiode. The markers hold the same meaning as described in **b)**.

where Φ is the radiant flux, z_0 the rest diameter of the artery and $R(z)$ the sum of the higher order terms in the expansion. The limit of this linearization is given by the maximum residual $\max[|R(z)|]$ which occurs at artery III in our simulations with $z_0 = 4.8$ mm and amounts to $\frac{\max[|R(z)|]}{\Delta\Phi_{norm}} \times 100\% = \frac{0.046}{0.56} \times 100\% = 8.3\%$ in case of infrared and $\frac{0.013}{0.32} \times 100\% = 4.2\%$ in case of red light. Both deviations are small enough to neglect $R(z)$ in Eq. (1), hence corroborating the linear approximation.

Sensitivity. The sensitivity of this linear measurement principle can be extracted from Eq. (1) as

$$c_\lambda = \frac{1}{\Phi(z_0)} \left. \frac{\delta\Phi(z)}{\delta z} \right|_{z=z_0}. \quad (2)$$

Table 1 reports the sensitivity values obtained from the simulations of three arterial rest diameters at two different wavelengths. From Table 1, it can be seen that the sensitivity depends on the rest diameter z_0 as well as on the wavelength λ of the light source.

Assuming the radiant flux decay to obey Beer's law, i.e. $\Phi(z) = \Phi(0)e^{-\mu_t z}$, where μ_t denotes the overall extinction coefficient of the artery, and substituting into Eq. (2) yields $c_\lambda = -\mu_t$. This explains on the one hand the negative value of c_λ and on the other the link between the sensitivity of the sensor system c_λ and the overall extinction coefficient of the artery μ_t and hence its wavelength dependence. However, the dependence on rest diameter cannot be explained

Table 1. Sensitivities for three different rest diameters at two wavelengths calculated as per Eq. (2) from the simulation data plotted in Fig. 1 (b).

model artery	simulated sensitivities	
	$c_{\lambda,660}$ (mm ⁻¹)	$c_{\lambda,880}$ (mm ⁻¹)
I ($z_0 = 2.42$ mm)	-1.30	-2.20
II ($z_0 = 3.35$ mm)	-1.07	-1.84
III ($z_0 = 4.81$ mm)	-0.91	-1.67

by Beer's law and shows the non-exponential form of the radiant flux decay, since a simple exponential yields a constant sensitivity for all rest diameters. Nonetheless, the sensitivity can be interpreted as an overall extinction coefficient of the artery that depends on the optical properties of the artery and its geometry.

Signal-to-noise. In a real sensor system performing transmission photoplethysmography, it is necessary that a sufficient number of photons reaches the photodetector in a short time, much shorter than the time scales of arterial distension. The term 'sufficient' here weights the number of photons reaching the photodetector and contributing to the signal current with respect to all sources generating noise current in the sensor system. In a realistic example, we consider an LED with an optical output power of 5 mW as light source, a typical photodetector with a responsivity of 0.5 A/W, and a dark current of 300 pA. Figure 1 (c) shows the maximum detected photocurrent by such a sensor system for the three aforementioned arteries at rest with diameters ranging from 2.4 to 4.8 mm. To highlight the effect of arterial diameter with respect to SNR, the plot shows one more artery with a diameter of 7.8 mm. For arteries with a diameter of 7.8 mm, the signal current at 660 nm is by a factor of 5 larger than the dark current of the photodiode, while the signal current of the infrared wavelength is below the dark current. This shows that the presented method is limited to arteries with diameters in the range of the human carotid artery of 5 – 7 mm and below [18, 19].

To sum up, an optimized sensor system is required to have a high signal-to-noise ratio, a high sensitivity and an excellent linear behavior over a wide range. As seen from the discussions above, these parameters are interdependent and necessitate trade-offs for optimum sensor design. In case of arterial diameters below 5 mm the infrared wavelength should be chosen because of the higher sensitivity, while for arteries with diameters above 6 mm the red wavelength range should be selected to achieve a reasonable SNR.

3. Sensor development

Since light source and photodetector have to be positioned directly at the artery, one major challenge is to design a sensor system that does not hinder the distension of the artery. For this purpose, a light weight, highly elastic sensor system was designed that establishes a smooth transition between the rigid mechanical properties of the optoelectronics and the soft mechanical properties of the distending artery. A 3D CAD drawing of this stretchable optoelectronic sensor design is presented in Fig. 2 (a).

The system is built up of two 16 μm thick polyimide (PI) substrates (see Fig. 2 (b)) with

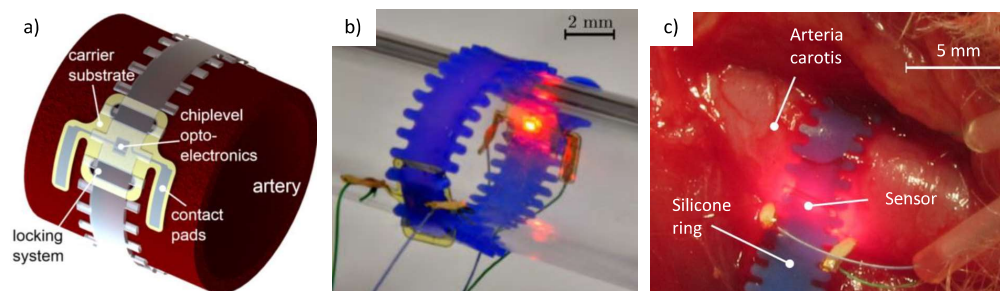


Fig. 2. **Sensor design and realization.** a) 3D model of the photonic sensor system wrapped around an arterial segment. b) Photo of a fully functional sensor wrapped around a glass tube. c) Sensor applied to the carotid artery of a sheep.

embedded electrical interconnects (600 nm Pt-Au-Pt) that contact the optoelectronics. The PI shell around the electrical interconnects serves as electrical passivation and makes the metal layers robust against twisting and bending [1]. A structured silicone ring (thickness 500 μm , Young's modulus 60 kPa at 0–30 % strain) aligns both PI substrates diametrically at the artery by a smart interlock design and keeps them in place during operation. For good visibility during *in vivo* experiments, the silicone ring is dyed blue as shown in Fig.2 (b) and (c). The optoelectronics consists of an LED (ELC-875-22, Jenoptik AG, Germany) as light source working at (875 ± 15) nm and a narrow-band photodiode (EPC-880-0.9-1, Jenoptik AG, Germany) as detector with a responsivity of 0.55 A/W in the infrared spectral range of (880 ± 58) nm. The narrow-band spectral matching reduces the influence of ambient light and improves the signal-to-noise ratio. The chip sizes of LED and photodiode are $650 \times 650 \times 180 \mu\text{m}^3$ and $860 \times 860 \times 300 \mu\text{m}^3$, respectively. The cleanroom steps to fabricate the PI substrates and to assemble and package the optoelectronic chips are adapted from recent developments in neural engineering [20] and were previously published by the same authors [2]. Further details on the sensor design and fabrication are given in Section 2 of the appendix.

4. In vitro validation

To establish the measurement principle and validate the theoretical findings, an artificial circulatory system was set up. The setup consists of a peristaltic pump mimicking the heart, two silicone tubes with diameters of 3.3 and 5 mm as artificial arteries, an oxygenator as lungs and erythrocytes in biological buffer as stabilized blood. An optical micrometer was used as reference measurement system for the absolute distension. From theoretical considerations, the infrared wavelength was chosen as the optimal wavelength for the sensor. Further details on the *in vitro* validation are given in Section 3 of the appendix.

Figure 3 shows the results obtained from the experiments with the 5 mm tube. Figure 3 (a) compares the reference measurement signal and the sensor output signal over two cycles of the artificial circulatory system. To obtain a signal which is proportional to the distension, Eq. (1) can be adapted for the measured output voltages $U_{PD}(t)$ from the photodetector and rewritten as

$$c_\lambda \tilde{u}(t) = \frac{U_{PD}(t)}{\max[U_{PD}(t)]} - 1, \quad (3)$$

where c_λ is defined as in Eq. (2), $\tilde{u}(t)$ corresponds to the distension $z - z_0$ and the measured voltage from the photodetector $U_{PD}(t)$ reflects the radiant flux $\Phi(z)$, while the residual $R(z)$ is omitted. Henceforth, the term $c_\lambda \tilde{u}(t)$ is denoted as scaled sensor signal. From Fig. 3 (a) it can be seen that the scaled sensor signal and the reference signal match perfectly. Figure 3 (b) investigates the linear correlation between both signals in a quantitative manner by plotting the scaled sensor signal against the optical micrometer reference data (blue dots). The linear fits with coefficients of determination of $R^2 = 0.9990$ for the 5 mm silicone tube and $R^2 = 0.9980$ for the 3 mm silicone tube explicitly establish the linearity of the sensor system as predicted by the simulation in Fig. 1 (b).

To analyze the linearity in a quantitative manner, simulations that perfectly match the experimental conditions of the *in vitro* experiments were carried out. The sensitivity of the sensor system is given by the slopes of the linear fits (black lines) of both the simulated data $c_{\lambda, \text{sim}}$ as well as the experimental data $c_{\lambda, \text{exp}}$ and are listed in Table 2 for two different diameters of the silicone tube. Table 2 shows that the simulations accurately predict the experimental sensitivity for different rest diameters of the silicone tubes.

Furthermore, the difference in sensitivity between a tube of rest diameter 3.3 mm and one of 5 mm is only 4.5 %. This underscores the weak dependence of the sensitivity on rest diameter. Hence, a rough estimate of the rest diameter of the implantation site allows for proper calibration of the sensor system. Due to this excellent quantitative agreement between simulated and

Table 2. Comparison of sensitivities. Experimental $c_{\lambda,exp}$ and corresponding simulation $c_{\lambda,sim}$ sensitivities obtained from Fig. 3 (b). The last column gives the deviation δ between simulated and experimental sensitivities.

silicone tube diameter \varnothing (mm)	simulated sensitivity $c_{\lambda,sim}$ (1/mm)	experimental sensitivity $c_{\lambda,exp}$ (1/mm)	deviation δ (%)
3.3	-1.32	-1.33	< 1
5	-1.25	-1.27	1.6

experimentally obtained sensitivities, the simulations can be used to calibrate the sensor system. Thus the arterial distension $\tilde{u}(t)$ in (mm) can be derived from the scaled sensor signal without use of empirical calibration methods based on look-up tables for c_{λ} .

To quantify the precision of the sensor system, the difference between arterial distension measured by the optical micrometer and determined by the optical sensor system calibrated via the simulation sensitivity $c_{\lambda,sim}$ is plotted as a histogram in Fig. 3 (c). The standard deviation of a Gaussian fit is used as measure for the precision of the sensor system and yields values of $4.5 \mu\text{m}$ in case of the 5 mm silicone tube and $6.4 \mu\text{m}$ in case of the 3.3 mm silicone tube. We want to point out that these deviations do not inherently arise due to the measurement principle but due to different waveforms at different measurement sites of the optical reference system and the developed sensor at the artificial circulatory system.

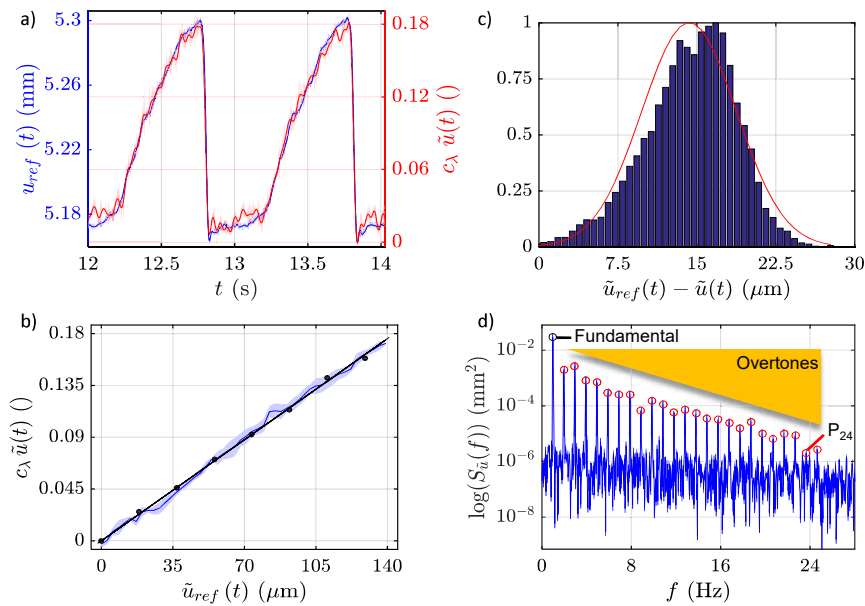


Fig. 3. **In vitro results.** **a)** Comparison of reference optical micrometer (blue) and scaled sensor (red) signals. The shaded areas represent the unfiltered signals, and the lines show filtered forms of the signals as guide to the eye. **b)** Scaled sensor signal plotted against the optical micrometer data (blue); the black line gives the linear fit with $R^2 = 0.9980$; the black dots show the simulation output. **c)** Deviation in distension between reference and sensor signals. The standard deviation of the gaussian fit (red) is $4.5 \mu\text{m}$ **d)** Power spectral density (blue) of the distension signal $\tilde{u}(t)$. The red circles depict the detected overtones and the black circle represents the fundamental frequency.

Another sensor characteristic to be evaluated is the sensor's resolution that is defined as the smallest detectable change in distension. To obtain this information, the optical sensor signal is analyzed in the frequency domain by its power spectrum shown in Fig. 3 (d). As the signal is composed of several harmonics, the smallest detectable overtone in this analysis corresponds to the smallest amplitude of the distension waveform. Hence, the resolution of the sensor system can be evaluated as a consequence of Parseval's theorem as

$$\Delta \tilde{u}(t) = \sqrt{\frac{S_{\tilde{u}}(f_L)}{\sum_{n=1}^N S_{\tilde{u}}(f_n)}} \times \max[\tilde{u}(t)], \quad (4)$$

where $\Delta \tilde{u}(t)$ is the resolution of the sensor system, $S_{\tilde{u}}(f)$ the power spectral density, f_L the frequency of the overtone with smallest amplitude, f_N the frequency of the last detectable overtone, and $\max[\tilde{u}(t)]$ the amplitude of the distension waveform. The resolutions obtained as per Eq. (4) are approximately 400 nm for the 3.3 mm tube and about 1 μm for the 5 mm tube. Here, we choose $f_L = 23.65$ Hz, $f_N = 24.63$ Hz for the 5 mm tube and $f_L = 38.24$ Hz, $f_N = 40.65$ Hz for the 3.3 mm tube. The resolution of the sensor system reduces with increasing rest diameter of the artery due to the decrease in sensitivity (see Table 2) as well as the reduced amount of photons reaching the photodetector at larger arteries.

5. In vivo experiments

To investigate the performance *in vivo*, the sensor system was wrapped around the left femoral artery of a sheep. To gain more parameters and complete the picture of the cardiovascular biomechanics, an intra-arterial tip catheter was used to measure the pressure inside the right femoral artery concomitantly. The hemodynamic state of the sheep during the experiments was altered by administering dopamine. Simulations specifically tailored towards the *in vivo* scenario of a sheep with a hematocrit of roughly 30 % reveal a sensitivity of $c_\lambda = -1.38 \text{ mm}^{-1}$ which is used to calibrate the optical sensor output over the entire experiment. To obtain absolute diameters, the rest diameter was measured using a caliper before the experiment started. Further details on the *in vivo* experiments are given in Section 4 of the appendix.

Figure 4 (a) shows the mean pressure signal $\bar{p}(t)$ (blue) and the measured rest diameter $u_0(t)$ (red) over 350 s, before [1], during [2] and after [3] administration of dopamine. As expected, the increase in intra-arterial pressure during activation of dopamine is accompanied by an increase in arterial rest diameter. However, during relaxation after maximum pressure, the arterial rest diameter shows a delayed response. This can be attributed to vasodilation, a vasomotoric effect that reflects the ability of muscular arteries to change their rest diameter and hence to regulate blood pressure actively. The colored boxes in Fig. 4 (a) show the unfiltered intra-arterial pressure $p(t)$ and arterial distension waveforms $\tilde{u}(t)$ over two cardiac cycles. All graphs in Fig. 4 (a) show highly reproducible signals over the entire experiment. The fact that the arterial distension signal leads the intra-arterial pressure is due to the different implantation sites of pressure and distension, necessary to prevent crosstalk between the intra-arterial pressure tip-catheter and the optical sensor signal.

To gain more insights into the performance of the optical sensor system *in vivo*, we switch again to the frequency domain, see Fig. 4 (b). By using Eq. (4), the resolution of the sensor system calculated from the power spectrum in Fig. 4 (b) is 570 nm. Here, the maximum distension is $\max[\tilde{u}(t)] \approx 250 \mu\text{m}$ for which the overtone number 18 at around 33 Hz as smallest detectable overtone was used. The spectrogram in Fig. 4 (b) shows the sensor signal over the whole experiment as a time-frequency plot. The plot proves that the sensor system is able to detect power as well as frequency shifts of the overtones which describe the response of the arterial wall due to the stimulation by an intra-arterial pressure wave. This representation reveals again that the sensor system is capable of resolving high frequency components of the arterial distension

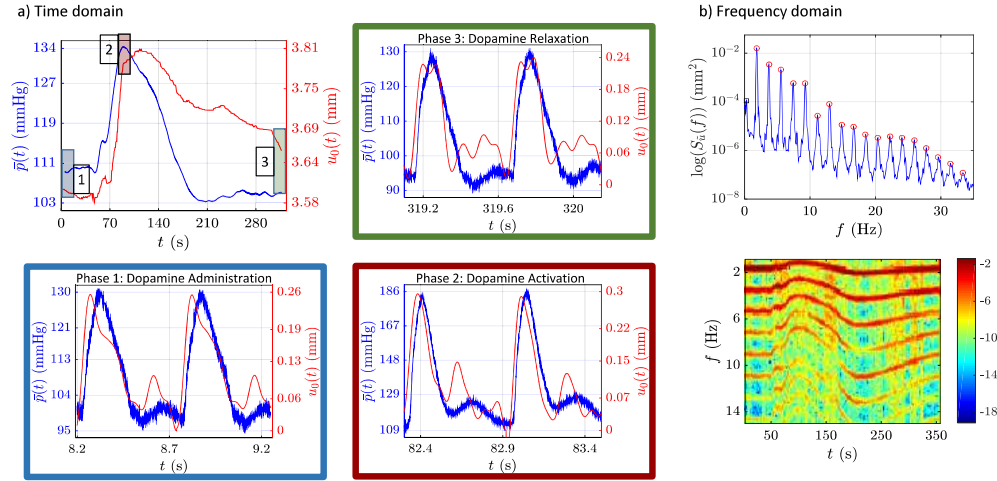


Fig. 4. *In vivo* results in time and frequency domain. **a)** Top left: Mean pressure $\bar{p}(t)$ (blue) and rest diameter $u_0(t)$ (red) over time during injection 1, activation 2, and relaxation 3 of dopamine. Colored boxes: Single pressure pulses (blue) and measured distension (red) in the three different phases of the dopamine experiment. **b)** Top: Power spectrum (blue) of the distension signal. The red circles indicate the detectable overtones in the distension signal. Bottom: Spectrogram showing the logarithmic power as a function of frequency and time over the entire experiment.

under extreme vital conditions. For informations on first experiments on biocompatibility of the sensor system the reader is referred to Ruhhammer et al. [21].

6. Arterial biomechanics

From a medical point of view, the most interesting application of the presented sensor system is to gain new insights into the biomechanics of the arterial tree and hence into various severe diseases such as arteriosclerosis, systemic hypertension, and cerebral or cardiac ischemic events that are directly linked to an increase in arterial stiffness. This section presents three ways to extract local as well as regional arterial stiffness measures from the highly resolved arterial distension waveforms [11, 13, 16].

Local arterial stiffness is measured by relating intra-arterial pressure and arterial distension, and quantifying the slope of this stress-strain relation by Peterson's modulus [22]. Figure 5 shows this stress-strain relationship over 10 cycles of the cardiovascular system for all three phases of dopamine administration, see Fig. 4. At high pressure in phase 2, Peterson's modulus increases to 109 kPa compared to values of 69 kPa and 78 kPa in phases 1 and 3, respectively. This clearly shows the non-linear elastic behavior of the arterial wall [11, 23]. The three different shapes of the stress-strain hystereses for the three regimes of the dopamine bolus indicate the ability of the arterial wall to change its dissipative nature on the timescale of seconds. A detailed quantification of the viscous parts of the arterial wall mechanics requires the identification of a biophysical model for the arterial wall and is addressed in future work. In particular, the highly reproducible stress-strain patterns over 10 cardiac cycles emphasize the stability and hence prove the precision of the measurement system *in vivo* under extreme vital conditions.

Regional arterial stiffness measures are of qualitative nature and exploit the strong correlation between the propagation speed of the pulse wave, known as pulse wave velocity (PWV) and the

average stiffness of the arterial segment over which the PWV is measured [24, 25]. In the case of a single sensor system, PWV can be approximated by the pulse arrival time (PAT), that is the period between the R-wave of the ECG and the arrival of the pulse wave at the measurement site defined by the maximum slope of the pulse wave, see inset in Fig. 5 (b). An increase in arterial stiffness causes an increase in PWV and hence a decrease in PAT. Figure 5 (b) shows the PAT in comparison with the systolic pressure over time. As expected, the PAT decreases as the systolic pressure increases, clearly indicating an increase in arterial stiffness which is in accordance with the results in Fig. 5 (a). By using two implants and measuring the distance between both sensor systems, PWV can also be measured directly. The advantage here is that the start and end point of the PWV measurement can be chosen arbitrarily, whereas ultrasound-based extracorporeal measurements of PWV are limited to superficial arteries such as the carotid and femoral artery.

One more way to gain insight into the state of disease of the cardiovascular system is to palpate the pulse and analyze its contour. Even though pulse-contour analysis is probably the oldest measurement technique of human physiology, it became more and more displaced with the development of blood pressure measurement systems providing systolic and diastolic pressures. However, recent advancements in the field of waveform sensing of arterial distension is shifting pulse-contour-analysis back into the focus of modern cardiovascular research [11, 13]. Figure 5 (c) shows arterial distension, velocity and acceleration over two pulses. All three physical quantities are in agreement with data published by other authors [11, 13], and show a high signal quality and hence, allow to extract the most important features of the pulse waveform, as the systolic foot, dichroic notch, augmentation index, and inflection point.

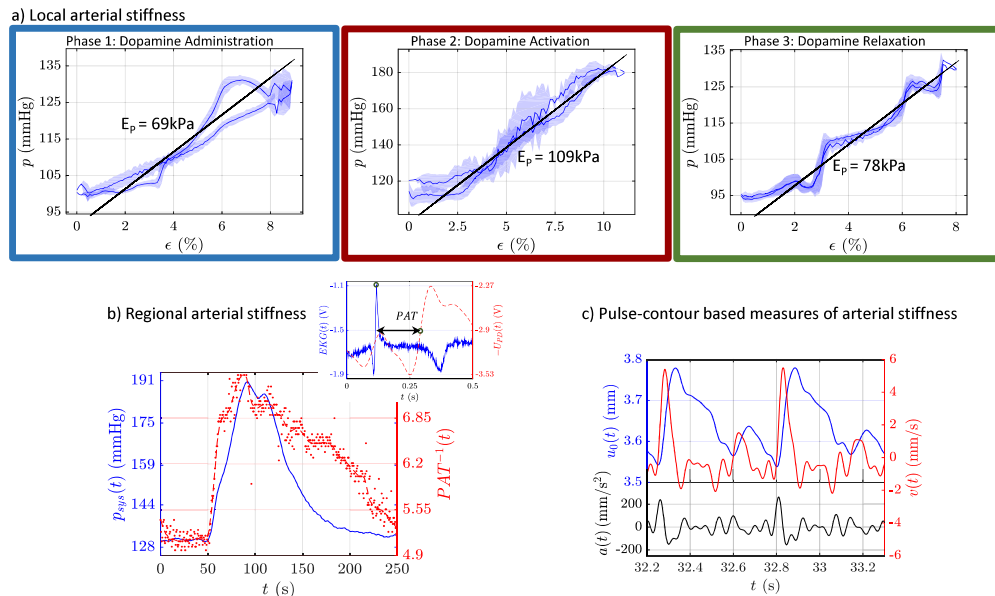


Fig. 5. Arterial stiffness. a) **Measurement of local arterial stiffness** Stress-strain-plots (blue shaded) and corresponding linear fits (black) that provide Peterson's modulus. The three subplots from left to right correspond to stress-strain plots evaluated from the signals from phases 1, 2 and 3 of Fig. 4, respectively. b) **Measurement of regional arterial stiffness.** Pulse arrival time (PAT) and systolic pressure p_{sys} over measurement time. The inset on the top left shows ECG and sensor signal to gain PAT. c) **Pulse contour-based arterial stiffness.** Plots show the arterial distension waveform u , the velocity v and acceleration waveform a , all obtained from the derivatives of the arterial distension waveform.

All these measures of arterial stiffness have their strengths and challenges. Local arterial stiffness provides the most direct and quantitative measure of arterial stiffness, but requires simultaneous monitoring of both pressure and distension. On the other hand, PWV and PAT provide a regional measure over larger segments of the arterial tree and hence may be a more versatile measure to correlate with cardiovascular disease pathology. In this context, arterial stiffness is determined indirectly and requires the implantation of two sensors. Finally, the strength of pulse contour analysis is that only one sensor is required. This configuration allows for example the estimation of arterial stiffness by measuring changes in reflected wave transit time (RWTT) [26]. So far, none of these measures has proven to be superior, and different measures are used depending on the application. In a nutshell, the high resolution, precision and signal-to-noise ratio of our sensor system allows to extract various quantities leading to the cardiovascular key parameter, arterial stiffness.

7. Conclusion

In this article, we presented a novel implantable, photonic sensor system to measure the small arterial distensions of about $250\mu\text{m}$ in vivo with a resolution below $1\mu\text{m}$, a precision of $5\mu\text{m}$, and a temporal resolution of 10 kHz. The presented photonic sensor system expands the toolbox of cardiovascular measurement techniques and shows the potential to measure key vital parameters continuously over the long-term. In the near term, this new approach offers a tool for clinical research, and as a perspective, a 24/7 monitoring system that enables novel diagnostic methods in arteriosclerosis and hypertension research that follow the trend in quantifying cardiovascular diseases by measurements of arterial stiffness and more generally pulse contour analysis.

Appendix

1. Optical simulations

The readers are encouraged to refer to Ruh et al. [17] and the corresponding references for a detailed description on how to model light propagation in large distending arteries. Table 3 lists the parameters of the simulation geometry while Tables 4 and 5 provide the intrinsic optical parameters of blood used for the red and infrared wavelength range, respectively.

Table 3. Simulation geometry. The radii of each artery were chosen to maintain a ratio of about 1.2 between outer and inner radius as found in most large arteries [24]. Furthermore, Young's modulus was chosen to achieve large arterial strains in the range of 6.5 to 10 %.

model artery	inner diameter r_i (mm)	outer diameter r_o (mm)	Young's modulus E_a (kPa)	maximum strain ϵ_{max} (%)
I	0.95	1.21	100	6.5
II	1.21	1.68	100	8.5
III	1.89	2.41	100	7.5
IV	3.08	3.81	100	10

Table 4. Intrinsic optical parameters of blood and arterial wall layers for $\lambda = 660$ nm. The optical parameters of blood were interpolated using the data and formulae given by Meinke [27] at a wall shear rate of 600 s^{-1} . The optical parameters of arterial wall layers are from Keizjer et al. [28]

$\lambda = 660 \text{ nm}$				
arterial layer	refractive index n	absorption coefficient μ_a (1/cm)	scattering coefficient μ_s (1/cm)	anisotropy factor g
adventitia	1.36	5	220	0.81
media	1.38	2	310	0.9
intima	1.39	3.25	190	0.85
blood	1.4	1.27	913.77	0.9752
ambient	1.33	0	0	1

Table 5. Intrinsic optical parameters of blood and arterial wall layers for $\lambda = 880$ nm. The optical parameters of blood were interpolated using the data and formulae given by Meinke [27] at a wall shear rate of 600 s^{-1} . The optical parameters of arterial wall layers are from Keizjer et al. [28].

$\lambda = 880 \text{ nm}$				
arterial layer	refractive index n	absorption coefficient μ_a (1/cm)	scattering coefficient μ_s (1/cm)	anisotropy factor g
adventitia	1.36	4	195	0.85
media	1.38	1.7	250	0.9
intima	1.39	2	150	0.85
blood	1.4	5.28	798.54	0.9745
ambient	1.33	0	0	1

2. Sensor design and technology

The cleanroom processes to fabricate the polyimide substrates, the assembly and packaging to electrically connect the optoelectronics in a robust way on the polyimide substrates, and the integration into silicone are detailed in this section. Both the fabrication processes as well as the assembly and packaging are based on an article published by Ruh et al. [2]. Any mention of commercial products or services is for experimental clarity and does not signify an endorsement or recommendation by the University of Freiburg.

Technology:

- Step 1** 1st spin coating step. First, an 8 μm thick polyimide (U-VARNISH-S; UBE America Inc., USA) layer is spin-coated onto a polished silicon handle-wafer at 2000 rpm for 30 seconds. Afterwards, a solvent (n-methyl-2-pyrrolidone) evaporation step is performed at 120 °C for 3 minutes. The spin-coated polyimide layer requires a curing step of 10 min at 450 °C in nitrogen atmosphere to avoid bubble formation and delamination.
- Step 2** Lift-off structuring of Pt-Au-Pt interconnects. Subsequently, a 7 μm thick layer of the negative photoresist AZnLOF 2070 (MicroChemicals GmbH, Germany) is spun onto the cured polyimide for 30 seconds at 3000 rpm and soft-baked at 100 °C for 7 minutes. After I-line exposure through a foil mask at 4.5 mW/cm² for 90 seconds, a one minute long post-exposure-bake at 110 °C is applied to the wafers. The development in AZ-726-MIF (MicroChemicals GmbH, Germany) takes 3.5 minutes. The exact compliance with the development time is crucial for this step in order to avoid resist delamination from the polyimide surface. A Pt-Au-Pt interconnection layer with film thicknesses of $t_{Pt1} = 50 \text{ nm}$, $t_{Au} = 400 \text{ nm}$ and $t_{Pt2} = 150 \text{ nm}$ is evaporated and structured by lift-off in acetone. Platinum serves as adhesion promoter to polyimide and as etch stop for later processes, whereas Au provides the better electrical conductivity. After lift-off, an ultrasonic cleaning of the wafers in acetone and isopropyl alcohol, as well as rinsing in deionized water is performed.
- Step 3** 2nd spin-coating step. Subsequently a second polyimide layer is deposited as described above.
- Step 4** Reactive Ion Etching (RIE) of polyimide. As a protective layer for the subsequent RIE step, a 28 μm thick layer of AZ 9260 (MicroChemicals GmbH, Germany) photoresist is deposited in a two-step spin-coating process for 30 seconds at 1600 rpm each. A 14 minutes long softbake at 100 °C is carried out after each step. Subsequent multiple exposure is done at 9 mW/cm² in six steps of 15 seconds with waiting times of 50 seconds between the steps, to reduce solvent evaporation and delamination of the resist. The subsequent development takes 8 minutes in 1:3 water-diluted AZ-400K (MicroChemicals GmbH, Germany). The contact pads are opened and the chips are diced simultaneously via RIE in oxygen plasma (200 W, 50 sccm, 30 mTorr). The measured etching rate of 370 nm/min can vary depending on the RIE equipment. After removal of remaining resist in acetone and ultrasonic cleaning of the wafers as described above, the diced foils can be easily peeled off by tweezers.

Assembly and packaging:

After stamping a conductive epoxy glue based on Araldite 2020 (Huntsman Advanced Materials) onto the exposed connector pad, the optoelectronics is positioned using die bonding (Tresky T-3002, Dr. Tresky AG, Switzerland). The top side contact is routed to the polyimide substrate via microflex interconnect (MFI) technology (introduced by Rubehn et al. [20]), as shown in Fig. 6. The basic idea behind MFI is given in the following. A small polyimide strip containing a Pt-Au-Pt track with a loop of 60 μm in diameter at its end is cut out of the contact pad for

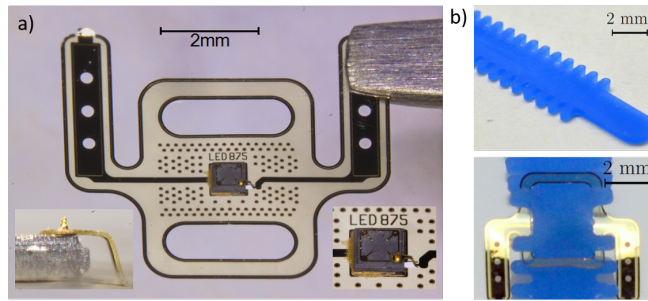


Fig. 6. Assembly and packaging. a) Polyimide sensor foil with an electrically interconnected infrared LED. The bottom side contact of the LED is interconnected to the substrate via an Araldite 2020 (Huntsman Advanced Materials, Germany) based conductive glue. The top side contact, shown in both insets, is connected by MFI technology [20]. b) Silicone strips with ripple structures adjust the two diametrically opposed polyimide foils by self-alignment around the blood vessel. For better visualization during *in vivo* experiments, blue pigment (NEUKASIL SN2490, Altropol Kunststoff GmbH, Germany) was added to the silicone. The picture on the bottom highlights the principle of the mechanical interlock between the silicone ripples and the polyimide sensor foil.

the backside contact of the optoelectronic chip during RIE and bent up by tweezers. A gold bump with a small tail of approximately $40\ \mu\text{m}$ is placed onto the bond pad of the optoelectronic chip by a ball and wedge bonder. The polyimide loop is pulled over the small tail and fixed with another gold bump.

A droplet of a biocompatible, optical epoxy adhesive (EPO-TEK 302, Epoxy Technology, Inc., USA), placed on top of the electrically interconnected chip, serves as robust package for the optoelectronics. Very thin biomedical grade wires with thread-like mechanical properties (35N-LT-DFT-28 Ag, Fort Wayne Metals Ireland Ltd) are used to connect the sensor system to the peripheral electronics, i.e. the laser driver for the LEDs and the transimpedance amplifiers to condition the photocurrent.

Integration in silicone:

Figure 6 (b) shows a flexible and stretchable strip of NEUKASIL RTV 23 (Altropol Kunststoff GmbH, Germany) silicone, which allows an easy self-alignment fixture of both fully assembled polyimide substrates on a blood vessel. The strip is pulled through the hooks in the polyimide foil, in which the ripple structures build a strong, but reversible physical interlock. The second sensor half is fixed in the same way on the opposite side of the blood vessel. The strengths of this concept are on the one hand the independence of arterial diameter, and on the other hand the capability to align both polyimide substrates diametrically at the artery. The silicone strips, shown in Fig. 6 (b), are fabricated within a molding process.

In the first step, a 100:4 mixture of the RTV 23 monomer with the corresponding cross linker (NEUKASIL A 7, Altropol Kunststoff GmbH, Germany) is prepared. For better visualization of the strips in *in vivo* experiments, blue color paste (NEUKASIL SN2490, Altropol Kunststoff GmbH, Germany) is added to the mixture. To avoid air bubbles, the mixture is evacuated at 0.5 mbar for 10 minutes. After that, the liquid material is transferred into an aluminum mold form by a squeegee and again evacuated for 10 minutes under 0.5 mbar. The following thermal cross-linking of the silicone takes 15 minutes at 90°C .

To ensure that the silicone strip does not hamper the arterial distension, we measured Young's modulus of the silicone. The data are presented in Fig. 7. The stress-strain data were measured in accordance with DIN 53504 with an experimental setup from Zwick GmbH & Co. KG. The graph

clearly shows that the silicone remains linear elastic up to strains of 200 %. Young's modulus was found to be 60 kPa in this range. Hence, it is guaranteed that the silicone does not hinder the distension of arteries with Young's moduli in the order of several hundred kPa.

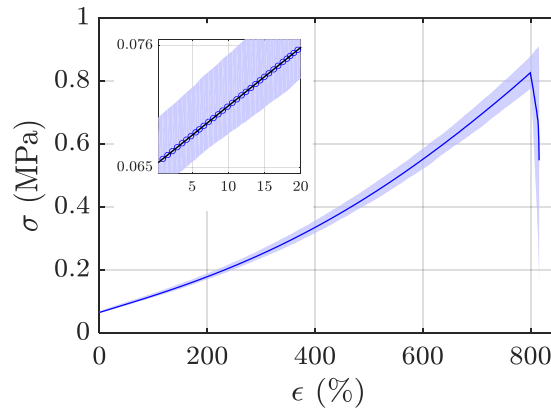


Fig. 7. Stress-strain plot of silicone RTV23. The material employed in our sensor strips was measured in accordance with DIN 53504 with an experimental setup from Zwick GmbH & Co. KG. The inset zooms into the stress response between 0 – 20 % strain. The shaded area reflects the minimum and maximum values of three measurements.

3. In vitro methods

Artificial circulatory system:

To mimic the cardiovascular system *in vitro* and to test the sensor properties and performance, we set up an artificial circulatory system. The setup shown in Fig. 8 was used for all *in vitro* experiments. It consists of a peristaltic pump (Ecoline VC-380, Ismatec Laboratoriumstechnik GmbH, Germany) with a resolution of 0.175 Hz. A silicone tube with an outer diameter of $\varnothing_1 = 3.3$ mm, wall thickness of $t = 0.4$ mm and a second tube of outer diameter $\varnothing_2 = 5$ mm, wall thickness of $t = 0.5$ mm were employed as measurement samples. Sheep blood in Alsevers buffer solution prepared using SOP CH50 at the University Medical Center's department of Rheumatology and Clinical Immunology in Freiburg was used as representative liquid. To maintain the oxygenation of blood, a blood oxygenator (hlite 800 LT Oxygenator, Medos Medizintechnik AG, Germany) with a maximum flow rate of 0.8 l/min was used. Blood was characterized with respect to hematocrit and oxygen saturation using a whole blood oximeter (Avoximeter, International Technidyne Corp, New Jersey, USA). To instantaneously measure the diameter of the silicone tubes, an optical micrometer (Optocontrol ODC-2600, $\mu\epsilon$ Messtechnik GmbH, Germany) as reference is employed. The resolution of this reference system is ± 1 μm . An infrared sensor was placed as shown in Fig. 8, its LED was driven at 15 mA. A transimpedance amplifier with a gain of 113 dB and a cutoff frequency of 4.5 KHz at 3 dB was used to amplify the sensor signals. Data recording was performed via a data acquisition card (NI USB-6251, National Instruments, USA) capable of simultaneously recording 8 channels with a maximum data transfer rate of 1.25 MS/s at a sampling rate of 100 KHz. The physiologically relevant parameters affecting the intrinsic optical parameters of blood are listed in Table 6 and remained stable over the entire measurement time. To model these *in vitro* conditions, we performed new simulations in which the intrinsic optical parameters were derived from empirical equations given by Meinke [27], as listed in Table 7. The exact simulation geometry is extracted from the data of the optical micrometer and is part of Table 8.

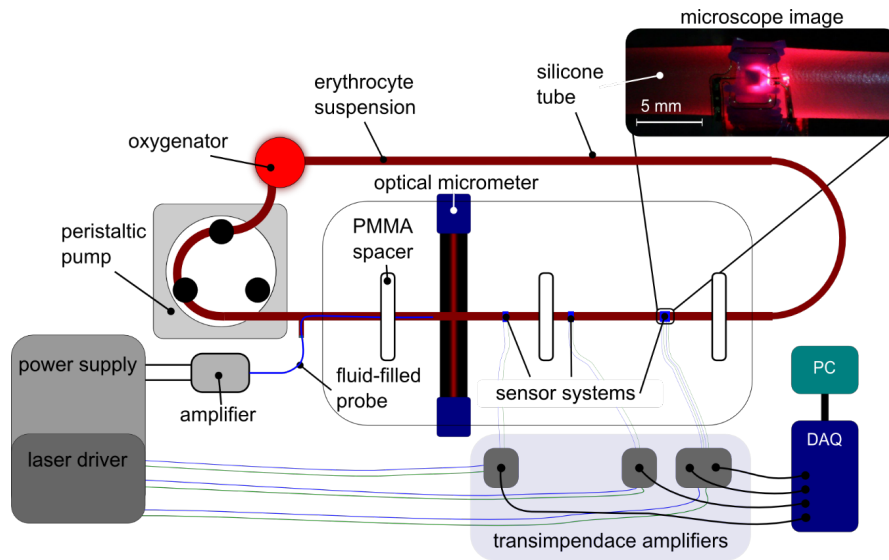


Fig. 8. Schematic of the artificial circulatory system. The figure shows the placement of the sensors and the optical micrometer, as well as various peripheral devices.

Table 6. Physiological parameters of erythrocytes in buffer used for *in vitro* experiments.

hematocrit	oxygen saturation	carboxyhemoglobin fraction	methemoglobin fraction
HCT (%)	SpO_2 (%)	$fCOHb$ (%)	$fMetHb$ (%)
23	99.8	1.9	0.8

Table 7. Intrinsic optical parameters of the various layers of the *in vitro* experiments. The intrinsic optical parameters of erythrocytes in buffer were extracted from Meinke [27] according to the physiological conditions provided in Table 6.

$\lambda = 880 \text{ nm}$				
	refractive index	absorption coefficient	scattering coefficient	anisotropy factor
	n	μ_a (1/cm)	μ_s (1/cm)	g
silicone	1.4	0	0	1
blood	1.35	2.88	633	0.982
ambient	1.33	0	0	1

Table 8. Simulation geometry extracted from the optical micrometer data used for modeling the *in vitro* experiments.

tube diameter due to datasheet	minimum tube diameter measured	maximum tube diameter measured	wall thickness
\varnothing (mm)	$\min[u_{ref}(t)]$ (mm)	$\max[u_{ref}(t)]$ (mm)	$r_o - r_i$ (mm)
3.3	3.92	4.14	0.4
5	5.2	5.33	0.5

4. *In vivo* amendments

In vivo simulation parameters:

Tables 9 and 10 provide the simulation input parameters to obtain realistic *in vivo* simulations.

Table 9. Simulation geometry of the femoral artery for modeling the *in vivo* conditions.

arterial diameter d (mm)	segment length l (mm)	intima thickness d_i (μm)	media thickness d_m (μm)	adventitia thickness d_a (μm)
3.41	5	109	275	150

Table 10. Intrinsic optical parameters of the various layers of the femoral artery to model the *in vivo* physiological conditions.

	$\lambda = 880 \text{ nm}$			
	refractive index n	absorption coefficient μ_a (1/cm)	scattering coefficient μ_s (1/cm)	anisotropy factor g
adventitia	1.36	4	195	0.85
media	1.38	1.7	250	0.9
intima	1.39	2	150	0.85
blood	1.39	3.76	731	0.98
water	1.33	0	0	1

Acknowledgements

The authors gratefully acknowledge Prof. Jens Timmer for fruitful discussions. The article processing charge was funded by the German Research Foundation (DFG) and the University of Freiburg in the funding programme Open Access Publishing.